Nanocrystalline Sm0.5Sr0.5CoO3−δ synthesized using a chelating route for use in IT-SOFC cathodes: Microstructure, surface chemistry and electrical conductivity

ARTICLE *in* JOURNAL OF SOLID STATE CHEMISTRY · FEBRUARY 2014

Impact Factor: 2.13 · DOI: 10.1016/j.jssc.2013.10

Journal of Solid State Chemistry 210 (2014) 53–59

Contents lists available at ScienceDirect

Journal of Solid State Chemistry

journal homepage: www.elsevier.com/locate/jssc

Nanocrystalline $Sm_{0.5}Sr_{0.5}CoO_{3-\delta}$ synthesized using a chelating route for use in IT-SOFC cathodes: Microstructure, surface chemistry and electrical conductivity

Rares Scurtu [a,b], Simona Somacescu [a,*], Jose Maria Calderon-Moreno [a], Daniela Culita [a], Ion Bulimestru [c], Nelea Popa [c], Aurelian Gulea [c], Petre Osiceanu [a]

[a] "IlieMurgulescu" Institute of Physical Chemistry, Romanian Academy, 202 SplaiulIndependentei, 060021 Bucharest, Romania
[b] Romania National Institute for Research and Development in Microtechnologies(IMT), 023573 Bucharest, Romania
[c] Faculty of Chemistry and Chemical Technology State University of Moldova 60 Mateevici, Chisinau MD 2009 Republic of Moldova

ARTICLE INFO

Article history:
Received 3 July 2013
Received in revised form
23 October 2013
Accepted 25 October 2013
Available online 5 November 2013

Keywords:
Cathode
Perovkites
Electrical conductivity
XPS
IT-SOFC

ABSTRACT

Nanocrystalline $Sm_{0.5}Sr_{0.5}CoO_{3-\delta}$ powders were synthesized by a chelating route using different polyfunctional H_xAPC acids (APC=aminopolycarboxylate; $x=3$, 4, 5). Different homologous aminopolycarboxylic acids, namely nitrilotriacetic (H_3nta), ethylenediaminetetraacetic (H_4edta), 1,2-cyclohexanediaminetetracetic (H_4cdta) and diethylenetriaminepentaacetic (H_5dtpa) acid, were used as chelating agents to combine Sm, Sr, Co elements into a perovskite structure. The effects of the chelating agents on the crystalline structure, porosity, surface chemistry and electrical properties were investigated. The electrical properties of the perovskite-type materials emphasized that their conductivities in the temperature range of interest (600–800 °C) depend on the nature of the precursors as well as on the presence of a residual Co oxide phase as shown by XRD and XPS analysis. The surface chemistry and the surface stoichiometries were determined by XPS revealing a complex chemical behavior of Sr that exhibits a peculiar "surface phase" and "bulk phase" chemistry within the detected volume (< 10 nm).

1. Introduction

Solid Oxide Fuel Cells (SOFCs) have attracted worldwide interest for their high energy conversion efficiency (50–70%), structural integrity, easy operation, low environmental impact and high tolerance to fuels [1–4]. Due to high operating temperatures and oxidizing atmosphere the cathodes used for SOFC require the use of noble metals, which are too expensive, or conducting metal oxides with transition metal ions which have multiple valences. The composition and microstructure of cathode materials have a large influence on the performance of solid oxide fuel cells (SOFCs) [5–7]. Careful design of materials composition through controlled oxygen nonstoichiometry can increase the ionic and electronic conductivities as well as the catalytic properties, associated to oxygen reduction in the cathode [8–10]. Significant efforts are focused on the development of intermediate-temperature (500–700 °C) IT-SOFCs. Sr-doped samarium cobaltite ($Sm_{1-x}Sr_xCoO_3$, SSC) is a promising cathode material for intermediate temperature (IT)-SOFCs because it shows high electrical conductivity even at intermediate temperature [11,12]. Different synthesis routes and different compositions have been developed in order to enhance the cathode performance, related to high surface-to-volume ratios, small grain size, porosity and crystalline phase [13–17]. Serra et al. [18] prepared cathode $La_{0.65}Sr_{0.3}MnO_3$ (LSM) and $La_{0.58}Sr_{0.4}Fe_{0.8}Co_{0.2}O_{3-\delta}$ (LSFC) materials by self-assembling method using an nonionic surfactant as template and spray-drying process adding Pd or Rh as promoters. They found that the preparation of relatively high surface area cathodes with enough thermal stability improves the oxygen exchange rate and therefore the overall SOFC performance.

Here we present $Sm_{0.5}Sr_{0.5}CoO_{3-\delta}$ powders synthesized by a chelating route using different chelating agents. We demonstrate the effects of the chelating agent on the structural, textural and electrochemical properties and discuss the different surface chemistry induced by the chelating agents. The electrical conductivity measurements demonstrate that the obtained ceramic powders are promising cathode materials for IT-SOFCs.

2. Materials and methods

2.1. Synthesis of materials

Our synthetic approach relied on the utilization of different polyfunctional H_xAPC acids (APC=aminopolycarboxylate; $x=3$, 4 or 5) to obtain the target heterometallic system, **$Sm_{0.5}Sr_{0.5}CoO_{3-\delta}$**. Accordingly, four homologous aminopolycarboxylic acids, namely nitrilotriacetic (**H_3nta**), ethylenediaminetetraacetic (**H_4edta**), 1,2-cyclohexanediaminetetracetic (**H_4cdta**) and diethylenetriaminepentaacetic

* Corresponding author. Tel.: +40 21 316 79 12; fax: +40 21 312 11 47.
E-mail address: ssimona@icf.ro (S. Somacescu).

0022-4596/$ - see front matter © 2013 Elsevier Inc. All rights reserved.
http://dx.doi.org/10.1016/j.jssc.2013.10.044

(**H_5dtpa**) were used as chelating agents to combine the three elements into a perovkite-type structure.

$Sm_{0.5}Sr_{0.5}Co$(nta) (SSCn): In this synthesis route cobalt(II) and strontium acetates were added to Sm(APC) aqueous solutions, obtained *in situ* by reacting stoichiometric amounts of Sm $(NO_3)_3 \cdot 6H_2O$ and corresponding H_xAPC acids, as follows: 3 mmol $Sm(NO_3)_3 \cdot 6H_2O$, 6 mmol H_3nta, 3 mmol $Sr(Ac)_2$, 6 mmol Co $(Ac)_2 \cdot 4H_2O$ and were successively added under vigorous stirring to 50 mL of distilled water at 70 °C. After all the reactants had completely dissolved, the reaction mixture was neutralized to pH ~ 7 with $NH_3 \cdot H_2O$. The resulting solution was treated with 2 mL of 5% H_2O_2 and slowly vaporized under continuous stirring until a dark purple dry powder was obtained. The last operation resulted in the color change of the reaction mixture from pink to purple, as a result of cobalt (II) to cobalt (III) oxidation. All the samples were calcined in air at 800 °C for 8 h. Similar synthesis routes were used with the substitution of H_4edta, H_4cdta $\cdot H_2O$ and H_5dtpa for H_3nta. The samples were labeled as following: SSCe, SSCc, SSCd.

2.2. Characterization of materials

X-ray diffraction (*XRD*) data were collected using parallel beam geometry on Rigaku's Ultima IV X-ray powder diffractometer,with Cu*K*α radiation ($\lambda = 1.54$ Å), operating at 40 kV and 30 mA, 0.02° step size and 5°/min scan speed.

Porosity analysis (*BET*) – Brunauer–Emmett–Teller adsorption–desorption isotherms of N_2 were obtained at 77 K over a wide relative pressure range from 0.01 to 0.995 with a volumetric adsorption analyzer TRISTAR 3000 manufactured by Micromeritics. The samples were degassed under vacuum for several hours at 423 K prior to nitrogen adsorption. Desorption isotherm was used to estimate the pore-size distribution.

Scanning electron microscopy (*SEM*): SEM measurements were carried out in a Field Emission Gun (FEG) FEI Quanta 3D microscope operating at 2 kV, equipped with an energy dispersive X-ray (EDX) spectrometer.

Surface analysis was performed by *X-ray photoelectron spectroscopy* (*XPS*) in a *PHI Quantera* equipment with a base pressure in the analysis chamber of 10^{-9} Torr. The X-ray source was monochromatized Al*K*α radiation (1486.6 eV) and the overall energy resolution is estimated at 0.65 eV by the full width at half-maximum (FWHM) of the Au4*f*7/2 photoelectron line (84 eV). Although the charging effect was minimized by using a dual beam (electrons and Ar ions) as neutralizer, the spectra were calibrated using the C1*s* line (BE = 284.8 eV) of the adsorbed hydrocarbon on the sample surface (C–C or (CH)n bondings). As this spectrum was recorded at the start and the end of each experiment the energy calibration during experiments was reliable.

The electrical conductivities were measured by AC *impedance spectroscopy*. The measurements were carried out with a Solartron 1260 FRA using a ProboStat sample holder (NorECs) heated up by Elite TSV12/50/300 furnace. The impedance spectroscopy measurements were conducted in air, in the temperature range of 20–950 °C, over the frequency range of 1 Hz–1 MHz and the amplitude of alternative signal was 100 mV. The temperature was acquired by using a Pt–Rh thermocouple located close to the sample.The powders were pressed under uniaxial pressure of ~100 MPa (~1 t/cm^2) and the resulted pellets were thermal treated in a furnace at 700 °C for 4 h in air. Heating rate was 10 °C/min. For a good contact with the electrodes, two Ag electrodes were pasted on samples surfaces and fired at 600 °C for 1 h. The experimental data were corrected for the stray capacitance of the sample holder and the resistance and inductance of the measuring leads by using Zview2 fitting software [19].

The specific conductivities of the samples were calculated from impedance data using the formula:

$$\sigma = \frac{t}{A \times R}$$

where *t* and *A* represent the thickness and area of the sample surface and *R* the electric resistance obtained from impedance spectra.

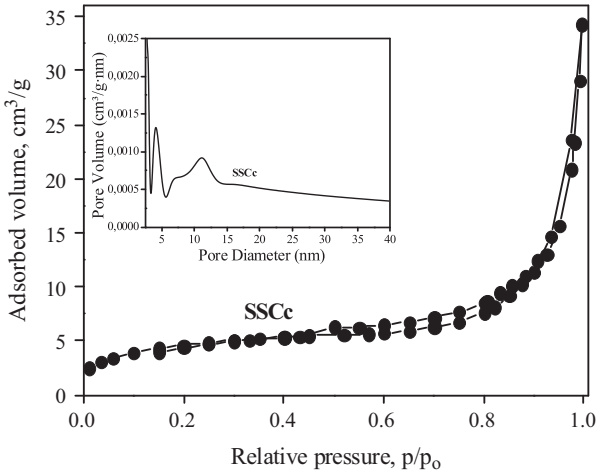

Fig. 2. N_2 adsorption/desorption isotherm and pore size distribution for SSCc sample.

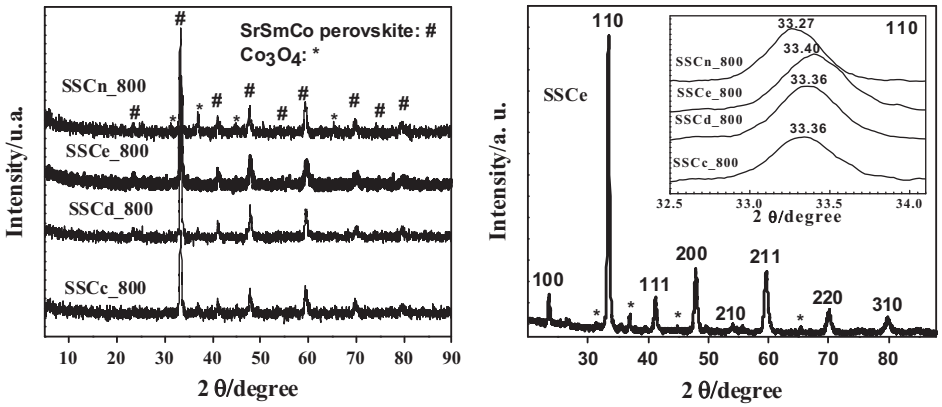

Fig. 1. (a) XRD patterns for SSCc, SSCd, SSCe, SSCn and (b) indexed pattern for SSCe; the inset shows the main SrSmCo perovskite peak for all the SSC powders.

3. Results and discussion

3.1. XRD

The powders XRD spectra (Fig. 1a), can be indexed in all cases to a cubic perovskite Samarium Strontium Cobalt Oxide $(Sm_{1-x}Sr_x)CoO_3$ (SSC) with lattice parameter 3.80(1) Å, with the presence of cubic Co_3O_4 (JPCDS Card no. 78-1969) as minor phase. The perovskite phase is isostructural with $SmCoO_3$ (JCPDS no. 75-0282), lattice parameter 3.75(1) Å, the incorporation of Sr into the cubic perovskite lattice results in the expansion of the cell volume due to the substitution of smaller Sm^{3+}, Co^{3+} ions ($Sm^{3+}\sim0.97$ Å; $Co^{3+}\sim0.75$ Å) by bigger Sr^{2+} ions ($Sr^{2+}\sim1.18$ Å).The inset in Fig. 1b shows the main 1 1 0 diffraction peak of the SSC powders, there are slight variations in the peak position of the SSC perovskite phase, attributed to compositional differences, detected by XPS measurements and discussed below. The crystallite sizes have been calculated by Scherrer's method from the peak width of the main XRD feature – (1 1 0) – at $\sim33.3^\circ$ (Fig. 1b), giving values of $\sim23\pm2$ nm for all the SSC powders.

Table 1
Summary of the textural properties.

Sample	S_{BET}	Adsorbed volume (cm^3/g)	Pore volume (cm^3/g)	Pore size (nm)
SSCc	15	35	0.0541	4; 13
SSCd	19	33	0.0461	11; 18; 38
SSCe	9	13	0.0214	8; 13
SSCn	25	35	0.0540	2; 4; 8; 12

3.2. BET

Fig. 2 shows the nitrogen adsorption/desorption isotherms of the SSCc sample and pore size distribution (inset Fig. 2). The same isotherm shape: type IV isotherm with type H1 hysteresis loops in the relative pressure range of 0.75–0.98, were obtained for all the samples. The absorption in this range at high relative pressure reveals a large pore size in the four samples. The average pore size distribution was determined from the desorption branch by the Barrett–Joyner–Halenda (BJH) method and shows a broad distribution in the range of 4–30 nm. The results of the BET measurements are presented in Table 1. A narrow pore size distribution was observed for the SSCc and SSCe samples. Although the SSCc sample shows a higher specific surface area, the pore sizes close to 4 nm are dominant, along with smaller contribution of pores larger than13 nm. The lowest value, measured for sample SSCe, can be explained by the narrow pore size distribution of the dominant pores centered at 11 nm and a lesser contribution of smaller pores, centered at 8 nm.

3.3. SEM

The SEM images of calcined $Sm_{0.5}Sr_{0.5}Co_{3-\delta}$ perovskite powders (Fig. 3) reveal a morphology of fine powders, with particle sizes ranging from ~60 nm in SSCd, ~150 nm in SSCc and SSCn, to ~200 nm in SCCe. The particles observed in SEM images are polycrystalline, the result of agglomeration of primary nanocrystallites. Higher contrast images of SSCe, obtained in BSE mode at low-voltage (2 kV), are shown in Figs. 4–6, clearly reveal the topography of the aggregates

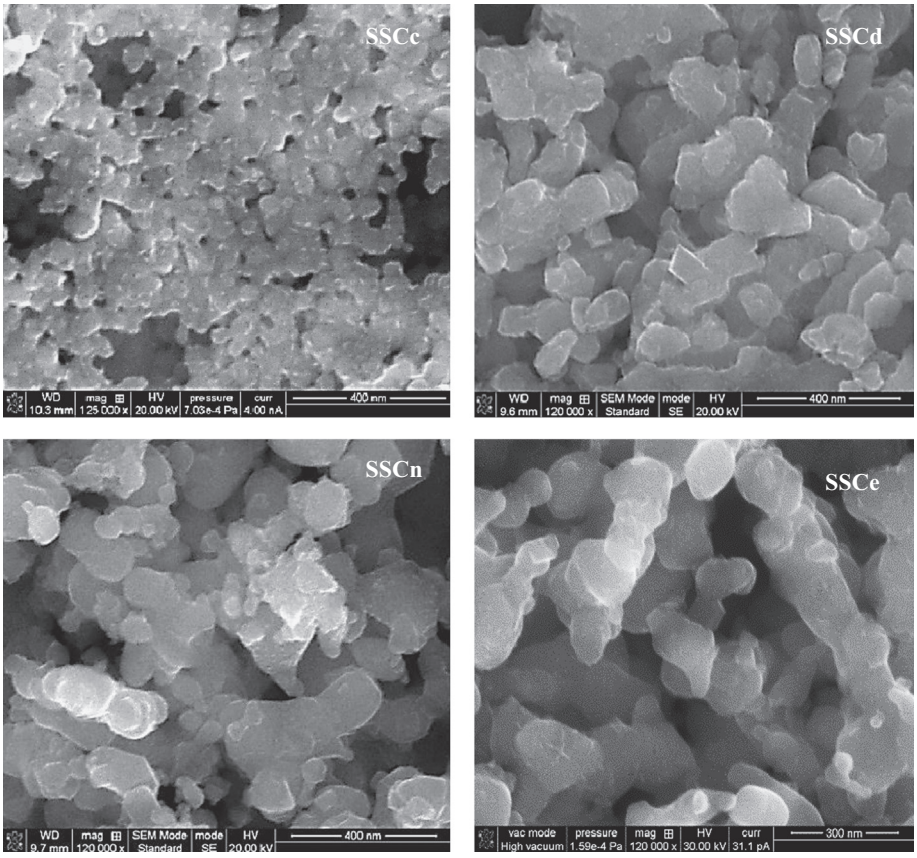

Fig. 3. SEM images for SSCd, SSCc, SSCe, SSCn.

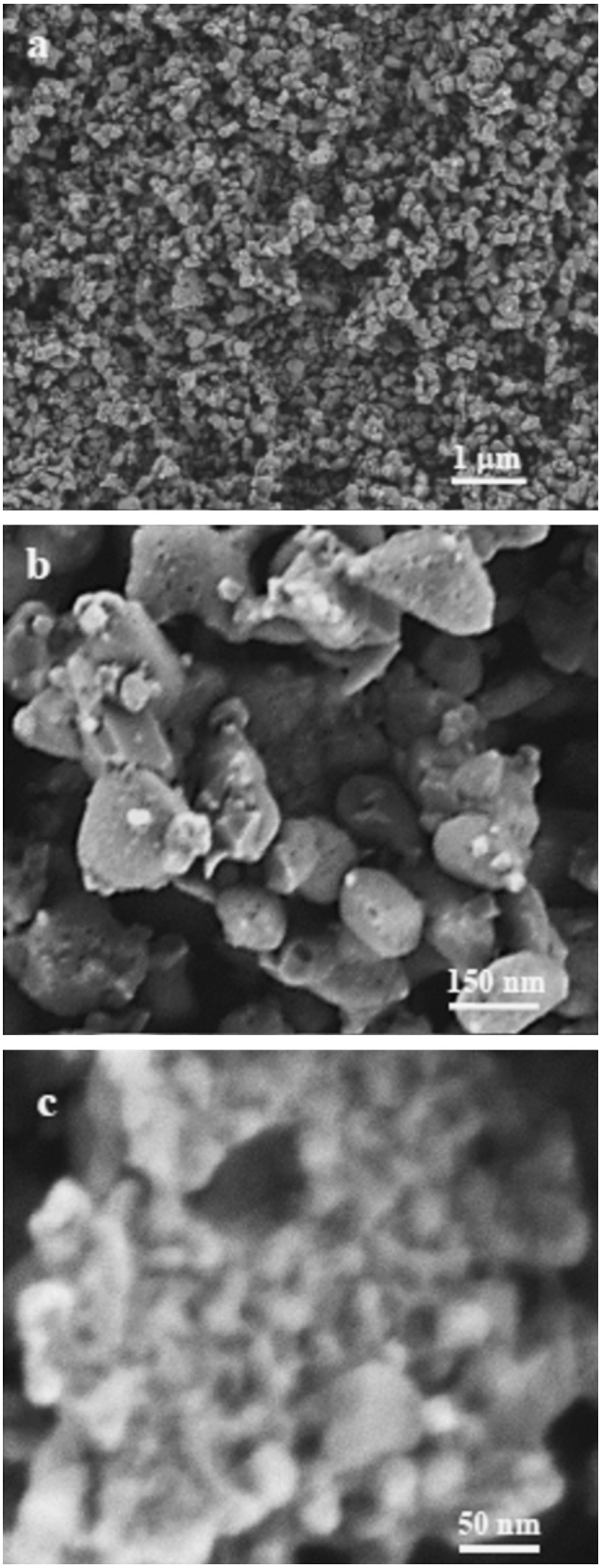

Fig. 4. Low voltage BSE image of SSCe.

observed in SE mode (Fig. 3), showing the nanosized porosity and the primary nanocrystallites, sized ~25 nm (Fig. 4b and c), forming the fine powder particles.

3.4. XPS results

After recording the general survey XPS spectra to detect all the elements present on the samples surfaces (at a depth < 10 nm) and the degree of surface contamination, high resolution spectra were collected on the most prominent XPS transitions: C1*s*, O1*s*, Sr3*d*, Sm3*d* and Co2*p*. Thus, the chemical species were determined as well as the surface stoichiometries by quantitative analysis of the perovskite-type ABO_3 associated with our samples. It is appropriate to note that the relative concentrations obtained by quantification were calculated with errors in the range of $\pm 10\%$, while the accuracy of the Binding Energies (BEs) assignments was estimated in the range ± 0.2 eV.

The high resolution superimposed spectra of Sm3$d_{5/2}$, Co2*p* are shown in Fig. 5, while the corresponding Sr3*d*, O1*s* spectra are displayed in Fig. 6 (a, c), respectively. A close inspection of these spectra reveal that the O1*s* and Sr3*d* regions exhibit a great complexity as a result of the mixture of different chemical environments. Complex angle resolved XPS investigations on similar perovskite-type oxides [20] evidenced a distinct "surface phase" (the outermost few monolayers, ~2–3 nm) and a "bulk-phase" (the following ~4–8 nm). Indeed, after spectral deconvolution the higher BEs (lower Kinetic Energies (KEs)) features for both O1*s* (Fig. 6d) and Sr3*d* band-like spectra (Fig. 6b) can be attributed to "surface-phase" while the features associated with lower BEs (higher KEs) are responsible for the "bulk-phase", as for example the 528.5 eV feature is assigned to bulk-bound O^{2-}. Similarly, to our knowledge, such low BEs for the Sr3*d* doublets [(127.3, 128.0), (129.3, 131.0) and (131.2, 132.8)] eV do not appear in the most cited databases [21,22].

The Co2*p* XPS spectrum shows the most prominent peak Co2$p_{3/2}$ at ~780.5 eV throughout.

These findings clearly evidence that Sr and at a less extent Sm exist in surface and bulk states, obviously the bulk states showing lower BEs (photoeletrons with higher KEs, and consequently larger escape depths). A similar trend exhibits O1*s* spectrum correlated to the above mentioned Sr, Sm behavior. In all cases, the elements detected at the outermost surface layer revealed higher BEs (lower KEs) than their bulk-lounded counterparts.

After quantification the following surface stoichiometries were experimentally determined (see Table 2). One can notice a clear tendency of Sr segregation towards the surface accompanied by Sm difussion from the surface to the bulk and consequently it results a disagreement between the nominal and experimental stoichiometries for the sample SSCn, revealing a surface enriched in Co and Sr oxides.

3.5. Electrical properties

Impedance spectroscopy measurements were made on pellets which were not fully densified, in order to measure the conductivity of samples similar to the real SOFC porous cathodes with three-phase-boundary (TPB) [23–25]. The electrical conductivities for our samples were determined relative to each other. The measured impedance spectra were similar for all investigated samples. The impedance spectra for SSCc sample, acquired in the temperature range of (227–927 °C) are presented in Fig. 7. From the representation of phase versus frequency we find out that the sample has a metallic-like behavior. The electrical resistances of samples were obtained from fitting experimental data using Zview [19] software. The electrical equivalent circuit which described, for the full range of frequencies, the electrical behavior of our samples, consisted in a series of a resistor, R and an inductance, L (due to the inductance effect of cables at higher frequencies).

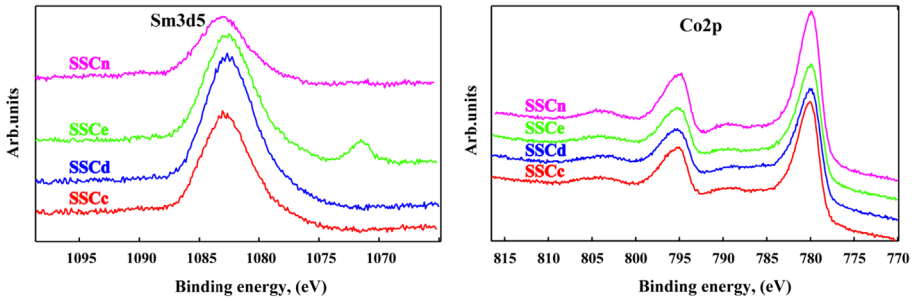

Fig. 5. The XPS superimposed high resolution spectra of Sm3$d_{5/2}$ (labeled Sm3d_5 hereafter) and Co2p for the samples.

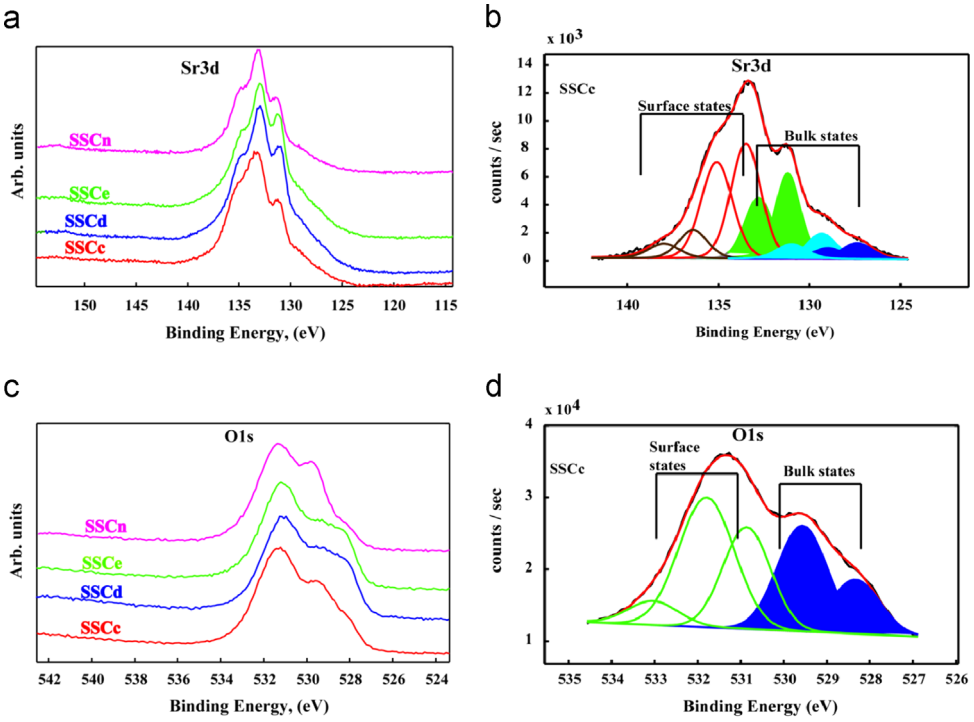

Fig. 6. The XPS superimposed high resolution spectra of Sr3d (a), O1s (c) and deconvoluted spectra of Sr3d (b), and O1s (d) in SSCc sample.

Tabel 2
XPS data: The binding energies and the experimental (surface) stoichiometries

Sample	Binding energy (eV)						Experimental surface stoichiometries
	O1s		Sr3$d_{(5/2;3/2)}$		Sm3$d_{5/2}$	Co2$p_{3/2;1/2}$	
	Surface	Bulk	Surface	Bulk			
SSCc	530.7 531.7 532.8 (61.5%)	528.3 529.5 (38.5%)	127.4; 129.0 129.3; 131.0 131.2; 132.8 (56.7%)	133.5; 135.1 136.3; 140.0 (43.3%)	1083.1	780.2, 795.3	$(Sr_{0.78}Sm_{0.25})Co_{0.92}O_3$
SSCd	530.8 531.6 532.9 (52.2%)	528.4 529.4 (47.8%)	127.5; 129.1 129.2; 131.0 131.3; 132.9 (51.5%)	133.6; 135.2 136.4; 140.1 (48.5%)	1083.3	780.3, 795.4	$(Sr_{0.9}Sm_{0.33})Co_{1.1}O_3$
SSCe	530.7 531.6 532.7 (51.3%)	528.2 529.4 (48.7%)	127.3; 128.9 129.3; 131.0 131.4; 133.0 (50.9%)	133.4; 135.0 136.4; 140.1 (49.1%)	1083.2	780.2, 795.4	$(Sr_{0.86}Sm_{0.27})Co_{1.22}O_3$
SSCn	530.9 531.8 532.9 (45.8%)	528.4 529.4 (54.2%)	127.5; 129.1 129.3; 131.1 131.2; 132.9 (54.8%)	133.5; 135.1 136.5; 140.2 (46.2%)	1083.2	780.3, 795.3	$(Sr_{0.5}Sm_{0.16})Co_{1.28}O_3$

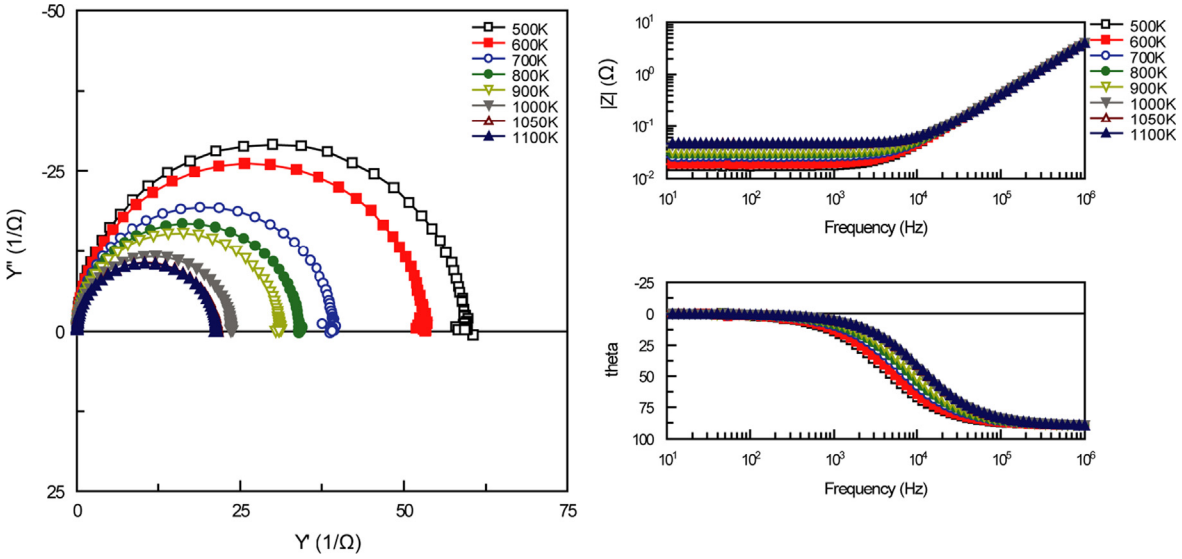

Fig. 7. Impedance spectra of SSCc samples (typical for all studied samples) measured at different temperatures in Nyquist representation (left) and in Bode representation (right).

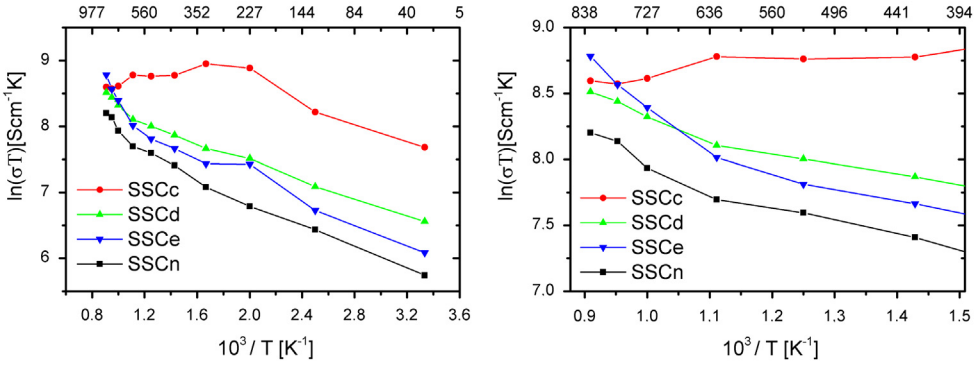

Fig. 8. The Arrhenius plots of total conductivities of all measured SSC samples (left) and the detailed view of them in the higher temperature range (right).

Fig. 8 shows the Arrhenius plots of the electrical conductivities for all samples measured in air and the detailed view of them in the high temperatures range. The sample SSCc exhibits electrical conductivities larger than the other samples for entire range of temperatures. At 700 °C, the typical working temperature for IT-SOFC, the SSCc sample displays the highest conductivity among our samples. Above 770 °C the sample SSCe exhibits even a higher conductivity but this behavior is due to its lower porosity shown by BET measurements. Since the SSCc reveals higher porosity coupled with a high conductivity lead us to the conclusion that this material shows a good electrical behavior. The small size of pores of SSCc sample can also contribute to its good electrical behavior because the smaller the pores the better the electrical contacts between the SSCc particles.

These results are in good agreement with the XPS measurements which have shown that SSCc presented the lowest concentration of Co oxide insulating phase on the surface of the powders. On the other hand, SSCn shows the highest concentration of Co oxide leading to the lowest values of the electrical conductivities on the entire range of temperatures. We must also notice a clear drop in Sm content on the surface which could be related to the diffusion/segregation phenomena leading to an enrichment in the Co oxide phase.

We can notice that the electrical properties were influenced by porosity and surface chemistry primarily induced by the H_xAPC acids (APC=aminopolycarboxylate; $x=3$, 4 or 5) used in the synthesis process. In fact, this aminopolycarboxylate have the ability to link the nitrogen atoms in order to increase the selectivity for a Sm, Sr, Co ions. The number of carbon atoms between the nitrogen and carboxyl group varies leading to a different arrangement of the substituents on the carbon atoms.

4. Conclusion

We prepared nanocrystalline $Sm_{0.5}Sr_{0.5}CoO_{3-\delta}$ powders by a chelating synthesis route, for use in IT-SOFC cathodes. The conductivities of our perovskite-type cathode materials depend on the nature of the precursor ligand, their values decreasing in the temperature range of interest (600–770 °C) such as: $\sigma_{SSCc} > \sigma_{SSCe} > \sigma_{SSCd} > \sigma_{SSCn}$. Nevertheless, in the narrow range (770–800 °C) the sample SSCe exhibits the highest σ values following the order: $\sigma_{SSCe} > \sigma_{SSCc} > \sigma_{SSCd} > \sigma_{SSCn}$. The structural and textural investigations by XRD, SEM,BET analysis highlighted a nanosized porosity and nanocrystallites sized ~25 nm forming the fine powder particles. A suitable pore size distribution was obtained by using ethylenediaminetetraacetic (H_4edta) and 1,2-cyclohexanediaminetetracetic (H_4cdta) as chelating agents (SSCe, SSCc sample). The surface chemistry and the surface stoichiometries were investigated by XPS method showing a complex chemical behavior of Sr that exhibits "surface phase" and "bulk phase" within the detected volume (< 10 nm). Although there is no direct link with the electrical properties such a complex behavior of the surfaces in our samples could be of great interest to explain the catalytic reactions that take

place at the cathod [9] (e.g. the adsorption of molecular oxygen and subsequent dissociation on the top of the surface). A correlation could be established between the electrical conductivity and the diffusion /segregation phenomena of Sr/Co leading to an enrichment in the insulating Co oxide phase. The catalytic properties of our synthesized cathode materials will be the subject of a further in-depth study.

In summary, by synthesis of cubic $Sm_{0.5}Sr_{0.5}CoO_{3-\delta}$ (SSC) perovskites with a high degree of purity, nanosized porosity, as well as by gaining a deeper insight in surface chemistry and stoichiometry would prove particularly beneficial for electrocatalytic performance of IT-SOFC cathodes.

Acknowledgments

The author Rareş Scurtu acknowledges the support of the Sectorial Operational Program Human Resource Development (SOPHRD) under the contract number POSDRU/89/1.5/S/63700. Further financial support by the Romania-Moldavia Republic Bilateral Cooperation (CB No. 416/2010) and the Partnership Program, contract 26/2012 are kindly acknowledged.

References

[1] J. Fergus, J. Fergus, X. Li, Solid Oxide Fuel Cells: Materials Properties and Performance, CRC, 2008.
[2] W. Vielstich, H. Yokokawa, H.A. Gasteiger, Handbook of Fuel Cells: Fundamentals, Technology, and Applications. Advances in Electrocatalysis, Materials, Diagnostics and Durability, part 5, Wiley, 2010.
[3] N.N. Brandon, D. Thompsett, Fuel Cells Compendium, Elsevier Science, 2005.
[4] S.C. Singhal, High-temperature Solid Oxide Fuel Cells: Fundamentals, Design and Applications: Fundamentals, Design and Applications, Elsevier Science, 2003.
[5] S. Huang, Q. Lu, S. Feng, G. Li, C. Wang, J. Power Sources 199 (1) (2012) 150–154.
[6] N. Li, Z. Lü, B. Wei, X. Huang, Y. Zhang, W. Su, Ceram. Int. 38 (3) (2012) 2159–2164.
[7] X. Ding, X. Kong, H. Wu, Y. Zhu, J. Tang, Y. Zhong, Int. J. Hydrogen Energy 37 (3) (2012) 2546–2551.
[8] D. Marinha, L. Dessemond, E. Djurado, J. Power Sources 197 (2012) 80–87.
[9] J.M. Serra, H.-P. Buchkremer, J. Power Sources 172 (2) (2007) 768–774.
[10] S. Pang, X. Jiang, X. Li, Q. Wang, Z. Su, Q. Zhang, Int. J. Hydrogen Energy 37 (5) (2011) 3998–4001.
[11] L. Yang, C. Zuo, S. Wang, Z. Cheng, M. Liu, Adv. Mater. 20 (17) (2008) 3280–3283.
[12] C.-H. Li, S.-H. Hu, K.-W. Tay, Y.-P. Fu, Ceram. Int. 38 (2) (2011) 1557–1562.
[13] L. Gómez, M.T. Colomer, J. Escobar, R. Moreno, J. Eur. Ceram. Soc. 33 (6) (2013) 1137–1143.
[14] G. Taillades, P. Batocchi, A. Essoumhi, M. Taillades, D.J. Jones, J. Rozière, Microporous Mesoporous Mater. 145 (1–3) (2011) 26–31.
[15] I. Hung, C.J. Ciou, Y.J. Zeng, J.S. Wu, Y.C. Lee, A. Su, S.H. Chan, J. Eur. Ceram. Soc. 31 (16) (2011) 3095–3101.
[16] C. Solís, V.B. Vert, M. Fabuel, J.M. Serra, J. Power Sources 196 (22) (2011) 9220–9227.
[17] V.B. Vert, J.M. Serra, J.A. Kilner, M. Burriel, J. Power Sources 213 (2012) 270–274.
[18] J.M. Serra, H.P. Buchkremer, J. Power Sources 172 (2) (2007) 768–774.
[19] D. Johnson, Zview, Scribner Associates, Inc., 2010.
[20] P. Van Der Heide, Surf. Interface Anal. 33 (5) (2002) 414–425.
[21] J.F. Moulder, W.F. Stickle, P.E. Sobol, K.D. Bomben, Handbook of X-ray Photoelectron Spectroscopy, Physical Electronics USA Inc., Minnesota, 1995.
[22] Alexander V. Naumkin, Anna Kraut-Vass, Stephen W. Gaarenstroom, C.J. Powell, NIST X-ray Photoelectron Spectroscopy Database, Version 4.1, 2012.
[23] E.V. Tsipis, V.V. Kharton, J. Solid State Electron. 12 (11) (2008) 1367–1391.
[24] J. Tolchard, T. Grande, J.Solid State Chem. 180 (10) (2007) 2808–2815.
[25] M. Bini, S. Ferrari, D. Capsoni, C. Spreafico, C. Tealdi, P. Mustarelli, J. Solid State Chem. 200 (2013) 70–75.